

# Pressure fluctuations and interfacial robustness in turbulent flows over superhydrophobic surfaces

J. Seo<sup>1</sup>, R. García-Mayoral<sup>1,2</sup>  
and A. Mani<sup>1</sup> †

<sup>1</sup>Center for Turbulence Research, Stanford University, Stanford, CA 94305, USA

<sup>2</sup>Department of Engineering, University of Cambridge, Cambridge CB2 1PZ, UK

(Received ?; revised ?; accepted ?. - To be entered by editorial office)

Superhydrophobic surfaces can entrap gas pockets within their grooves when submerged in water. Such a mixed-phase boundary is shown to result in an effective slip velocity on the surface, and has promising potential for drag reduction and energy saving in hydrodynamic applications. The target flow regime, in most of such applications, is a turbulent flow. Previous analyses of this problem involved direct numerical simulations of turbulence with the superhydrophobic surface modeled as a flat boundary, but with heterogeneous mix of slip and no-slip boundary conditions corresponding to the surface texture. Analysis of the kinematic data from these simulations has helped to establish the magnitude of drag reduction for various texture topologies. The present work is the first investigation that, alongside a kinematic investigation, addresses the robustness of superhydrophobic surfaces by studying the load fields obtain from DNS data. The key questions at the focus of this work are: does a superhydrophobic surface induce a different pressure field compared to a flat surface? How does this difference scale with system parameters, and when it becomes significant that it can deform the air-water interface and potentially rapture the entrapped gas pockets? To this end, we have performed direct numerical simulations of turbulent channel flows subject to superhydrophobic surfaces over a wide range of texture sizes spanning values from  $L^+ = 6$  to  $L^+ = 155$  when expressed in terms of viscous units. The pressure statistics at the wall are decomposed into two contributions, one coherent, caused by the stagnation of slipping flow hitting solid posts, and one time-dependent, caused by overlying turbulence. The results show that the larger texture size intensifies the stagnation pressure contribution, while the turbulence contribution is essentially insensitive to  $L^+$ . The two-dimensional stagnation pressure distribution at the wall and the pressure statistics in the wall-normal direction are found to be self-similar for different  $L^+$ . The scaling of the induced pressure and the consequent deformations of the air-water interface are analyzed. Based on our results, an upper bound on the texture wavelength is quantified that limits the range of robust operation of superhydrophobic surfaces when exposed to high speed flows. Our results indicate that when the system parameters are in terms of viscous units, the main parameters controlling the problem are  $L^+$  and a Weber number based on inner dimensions; We obtain good collapse when all our results are expressed in wall units, independently of the Reynolds number.

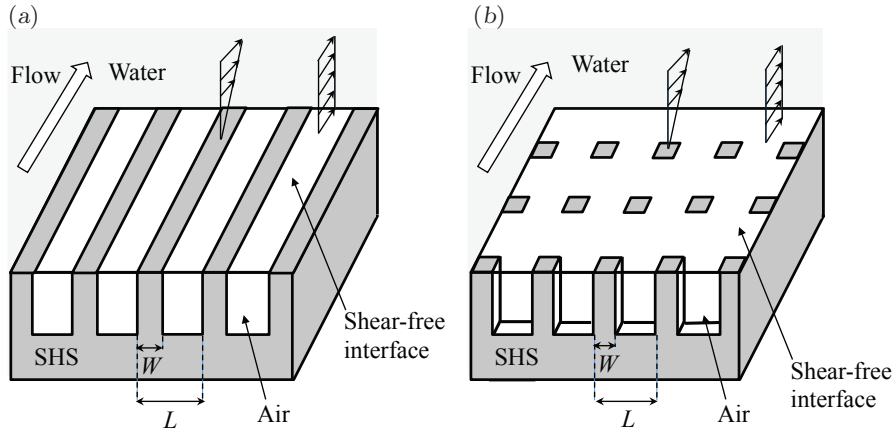


FIGURE 1. Schematic representation of a channel with superhydrophobic-surface boundary conditions on both walls, (a) streamwise-aligned ridges and (b) posts. Note that these representations do not exactly portray the arrangements studied, which have more texture features in the simulation domain than shown here.

## 1. Introduction

Development of methods and investigation of phenomena leading to skin friction drag reduction in turbulent flows has been an active area of research for several decades, and different strategies have been proposed and studied with mixed success. Of these, superhydrophobic surfaces for naval applications have received a great deal of attention recently. Superhydrophobicity enables textured surfaces immersed in water to entrap pockets (or bubbles) of air. The bubbles can lodge within the texture grooves, when the groove size is small enough. This is known as the Cassie-Baxter state (Cassie & Baxter 1944), in opposition to the fully-wetted, Wenzel state (Wenzel 1936), in which the surface cavities are filled with water and the hydrophobic effect is diffused away. Under Cassie-Baxter conditions, much of the overlying water flow is in contact with the entrapped air, and not with the solid surface. Thus, the air ‘layer’ acts as a lubricant for the outer flow, which can effectively slip over the wall, experiencing reduced friction compared to conventional, smooth surfaces (Rothstein 2010). The drag-reducing properties of superhydrophobic surfaces were first demonstrated for laminar flows (Watanabe *et al.* 1999; Ou *et al.* 2004; Choi & Kim 2006; Choi *et al.* 2006). Under turbulent conditions, Daniello *et al.* (2009) experimentally showed that superhydrophobic surfaces were able to achieve high drag reductions of up to at least 25%. Min & Kim (2004) studied the reduction for turbulent flows numerically, by modeling the effective hydrophobicity as a spatially-uniform slip length. They also studied the effect of these surfaces on the stability of the flow and the transition to turbulence (Min & Kim 2005). The assumption of a single, homogeneous slip length of Min & Kim (2004), analogous to the nanoscale Navier-slip effect of hydrophobicity (Thompson & Troian 1997; Freund 2003), implies that the surface texture modeled is isotropic. More recently, Busse & Sandham (2012) comprehensively investigated the effects of slip length anisotropy on turbulence statistics. The detailed geometry of the texture was first studied in simulations by Martell *et al.* (2009), who used a patterned slip/no-slip boundary condition to model the alternating contact with the entrapped air pockets and the roughness crests separating them.

Although the drag-reducing properties of superhydrophobic surfaces on turbulent flows

† Email address for correspondence: alimani@stanford.edu

have received a great deal of attention, both experimentally (Daniello *et al.* 2009; Woolford *et al.* 2009; Park *et al.* 2014; Bidkar *et al.* 2014; Srinivasan *et al.* 2015) and numerically (Min & Kim 2004; Martell *et al.* 2009, 2010; Park *et al.* 2013; Türk *et al.* 2014; Jelly *et al.* 2014), the interaction of these surfaces with the flow has not yet been fully investigated. The above cited numerical studies, for instance, have concentrated on the drag-reducing slip effect, without considering the problem of gas-liquid interface stability and bubble depletion. The drag reduction predicted by these studies increases with the size of the texture grooves, in agreement with the theoretical analyses of Lauga & Stone (2003), Fukagata *et al.* (2006), Belyaev & Vinogradova (2010), and Ybert *et al.* (2007), although the behavior deviates from the theoretical linear predictions for large textures. In real flows, however, the Cassie-Baxter state, and thus drag reduction, is completely lost for textures larger than a threshold size (Aljallis *et al.* 2013; Bidkar *et al.* 2014). Therefore, development of insights that can lead to optimal design of superhydrophobic textures, requires advancement of knowledge of flow-interface interactions, and mechanism of interface breakage when these surfaces are subject to turbulent flow conditions.

In this paper, we present the first investigation of such mechanisms by studying the pressure loads on the air-water interface. We intend to establish a clear distinction between the dynamical mechanisms related to the size of the texture and those related to the overlying flow being turbulent. We analyze with special emphasis the different scalings for both types of mechanisms. The purpose of such study is twofold.

First, we assess the validity of extrapolating the conclusions of numerical simulations to practical flows. Most experimental measurements reported, like those of Daniello *et al.* (2009) and Park *et al.* (2014), have been conducted at texture sizes of order  $L^+ \approx 0.5-5$ , where the ‘+’ superscript denotes scaling with the kinematic viscosity  $\nu$  and the friction velocity  $u_\tau$ . Although no clear reason has been given, it is likely that for larger textures the stability of the bubbles is lost, since they would otherwise yield larger drag reductions. In contrast, most of the numerical studies cited above have been conducted at  $L^+ \approx 10-200$ , and most often near the upper limit. This is frequently due to a compromise between computational cost and physical fidelity. However, these numerical simulations assume a stable and flat air-water interface, but it is unclear whether gas layer would remain stable at such large  $L^+$ . It is also questionable whether some of the dynamics that are reported in the large  $L^+$  range would be relevant at the smaller  $L^+$  values of real applications.

Second, we characterize deleterious effects that appear as  $L^+$  increases, leading to the degradation of the improving-with-size performance, and eventually to the complete loss of the superhydrophobic effect. Some work in this direction has begun to appear recently, but the mechanisms implicated in the degradation are still largely unknown. Steinberger *et al.* (2007), Hyvälöuoma & Harting (2008), Karatay *et al.* (2013), and Teo & Khoo (2010) have studied the effect of bubble shape when the interface is not perfectly flat, while Busse & Sandham (2013) have analyzed how the performance degrades as the height of the air layer decreases, and the texture crests begin to protrude out of it, introducing a roughness-like effect. Lee & Kim (2009), Patankar (2010), and Samaha *et al.* (2011) have analyzed the transition from the Cassie-Baxter to the Wenzel state through static pressure effects. Aljallis *et al.* (2013) have experimentally considered the effect of shear on bubble depletion at high Reynolds-numbers. Bidkar *et al.* (2014) examined different types of surface coating, changing chemical treatment and surface roughness size, and suggested that, for stable drag reduction at high Reynolds-numbers, the roughness height should be much smaller than viscous sublayer. Here we investigate the modulation with texture size of the pressure forces that act on the bubbles. As these forces increase with the texture size, they impose an upper limit on the possible texture dimensions, since for larger textures the air-water interface is not able to withstand the pressure forces for a

given finite surface tension. The pressure stresses on the interface may on their own be a direct cause for the interface instability as the texture size increases.

In direct relation to those pressure stresses, we study two types of geometrical patterns, two-dimensional ones aligned in the direction of the flow, or ridges, and three dimensional ones equally distributed along the streamwise and spanwise directions, or posts. A schematic of these geometries are shown in figure 1. Streamwise ridges have often been favored in experiments, while the posts would, according to the theoretical predictions, yield larger drag reductions for the same feature width. We will see that posts are more sensitive to pressure stresses as  $L^+$  increases. This may be a reason for choosing ridges when aiming to maximize the texture spacing, so the stability of the gas pockets is maintained. Nevertheless, studying the three dimensional post geometry is likely more relevant to practical applications, since most economically feasible methods of fabrication of superhydrophobic surfaces involves spray of material or similar processes that results in protrusion of post-like geometries on the surface, as opposed to streamwise structures.

The paper is organized as follows. In §2 we present the equations and discuss the key dimensions and dimensionless parameters for the problem. In §3 we outline the algorithms used to numerically solve that set of equations. The results of our simulations are presented and discussed in §4. Finally, our conclusions are summarized in §5.

## 2. Problem formulation

We consider the motion of a turbulent liquid flow in a doubly-periodic channel with superhydrophobic rough walls that have entrapped gas pockets, as sketched in figure 1. The roughness is made up by a streamwise- and/or spanwise-periodic patterned texture of period  $L$ . We assume that the flow is governed by the incompressible Navier-Stokes equations,

$$\nabla \cdot \mathbf{u} = 0, \quad (2.1)$$

$$\frac{\partial \mathbf{u}}{\partial t} + \mathbf{u} \cdot \nabla \mathbf{u} = -\nabla p + \nu \nabla^2 \mathbf{u}, \quad (2.2)$$

where  $\nu$  is the kinematic viscosity and the liquid density is  $\rho = 1$ .

The flow is bounded by protruding patterned elements and the gas pockets interspersed between them. No slip is assumed at the solid-liquid interfaces, and the air/water viscosity ratio is considered small enough so that the gas-liquid interface can be modeled by a free slip boundary condition. All the boundaries are impermeable, and we neglect the deformation of the gas-liquid interfaces in the simulations of the flow. This is the standard treatment in the literature for DNSs considering superhydrophobic textures (Min & Kim 2004; Martell *et al.* 2009, 2010; Busse & Sandham 2013; Park *et al.* 2013; Türk *et al.* 2014; Jelly *et al.* 2014). However, *a posteriori*, we calculate the deformation of the interface responding to the pressure difference from the DNS results, as an equivalent way of representing the pressure distribution on the wall. The deformation of the interface obeys the Young-Laplace equation,

$$\nabla^2 \eta \approx \frac{P_{liquid} - P_{gas}}{\sigma}, \quad (2.3)$$

where  $\sigma$  is the surface tension, and  $\eta$ , is interface height measured from the channel wall plane at  $y^+ = 0$ . Within the gas pockets, we assume  $P_{gas}$  is uniform, and governed by the mass conservation of the gas,

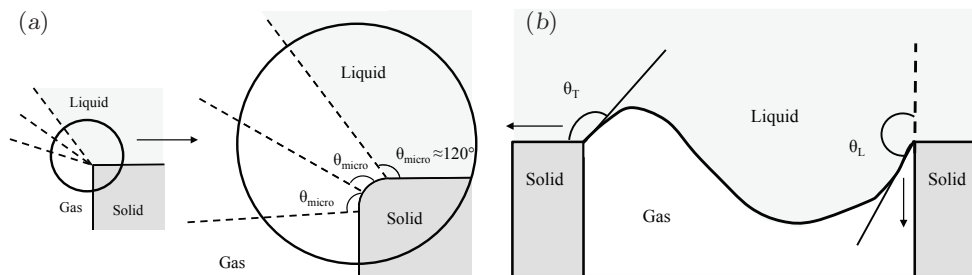


FIGURE 2. (a) Macroscopic corner angle and microscopic contact angles under the pinned interface assumption (b) Corner angles at trailing edge ( $\theta_T$ ) and leading edge ( $\theta_L$ ).

$$\iint \eta \, dx \, dz = 0. \quad (2.4)$$

The gas-liquid interface is assumed to be effectively pinned to the post edges, as shown in figure 2(a), which are macroscopically sharp but can be rounded on a microscopic scale. The microscopic contact angle,  $\theta_{\text{micro}}$ , can stay unchanged (or in between the nominal advancing and receding contact angles) while the macroscopic corner angles,  $\theta_T$  and  $\theta_L$ , may be altered, and allowed to adjust its contact point along the round corner. This assumption, together with the mass conservation of the gas, implies that the interface is never broken and the air bubbles are stably pinned inside the roughness. This assumption is reasonable as long as  $\theta_{\text{rec}} - \pi/2 < \theta_L < \theta_{\text{adv}}$  and  $\theta_{\text{rec}} < \theta_T < \theta_{\text{adv}} + \pi/2$ , where  $\theta_{\text{adv}}$  and  $\theta_{\text{rec}}$  are the microscopic advancing and receding contact angles respectively. Moreover, we will use such framework to predict the onset conditions leading to interface breakage.

The dimensional analysis of the problem reveals that the solution depends on a number of dimensionless parameters. The first is a Reynolds number based on the channel half-height, for instance the friction Reynolds-number  $\text{Re}_\tau = u_\tau \delta / \nu$ , which measures how ‘turbulent’ the flow is. For a realistic naval application with a moving object of dimensions of order  $\sim 1$  m and a velocity of order  $\sim 5$  m/s,  $\text{Re}_\tau$  is typically  $\sim 4000$ . This value is at present barely reachable by direct numerical simulation, even for smooth walls (Lee & Moser 2015; Lozano-Durán & Jiménez 2014). Instead, we run our simulations at more modest  $\text{Re}_\tau \approx 200$ -400, at which near-wall effects can still be correctly simulated (García-Mayoral & Jiménez 2012) at a more cost-effective expense.

Another important Reynolds-number is the size of the texture in viscous units  $L^+ = u_\tau L / \nu$ , which measures how much the flow deviates from a canonical, smooth-wall flow. For small  $L^+$ , the effect of the superhydrophobic surface can be treated as a perturbation for the buffer layer flow, while for large  $L^+$  the flow is completely modified and resembles more a flow around obstacles (Jiménez 2004). As mentioned above, typical experimental values are  $L^+ \lesssim 5$ . In the present work, we have investigated textures with sizes  $L^+ \approx 6$ -155. Our smallest surface wavelength can be applicable for the recent experimental studies and reaches practical limit. Previous numerical studies have used  $L^+$  values on the order of hundred (Martell *et al.* 2009, 2010; Busse & Sandham 2013; Türk *et al.* 2014; Jelly *et al.* 2014). In spite of the large slip velocities and drag reductions that they produce, such predictions are practically unrealistic since they do not incorporate gas layer stability considerations. The underlying reason is again that the resolution required for the simulation of smaller textures makes them very expensive, and such simulations are only beginning to appear (Türk *et al.* 2014). Results obtained at  $L^+ \approx 100$ -150 should be taken with caution, and only for the purpose of qualitative analysis.

The third dimensionless parameter involves the air-water interfacial surface tension. We

6

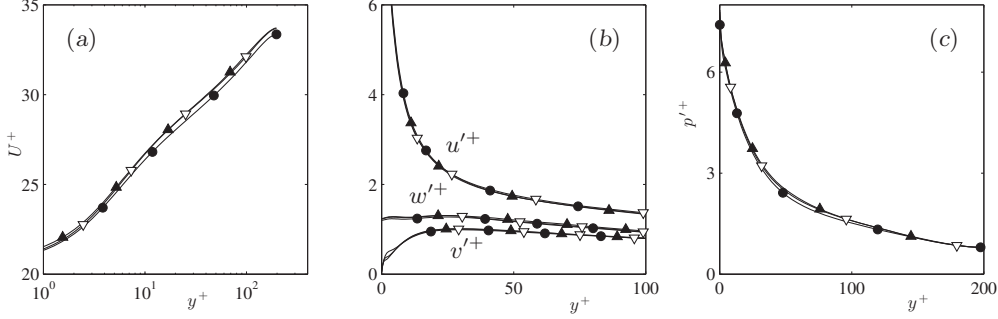
*J. Seo, R. García-Mayoral and A. Mani*

FIGURE 3. Resolution test for the post geometry with  $L^+ \approx 155$  at  $Re_\tau \approx 200$ . (a) Mean streamwise velocity profile; (b) velocity rms fluctuations; (c) pressure rms fluctuations.  $\bullet$ ,  $\Delta x^+ \approx 6.4$ ,  $\Delta z^+ \approx 3.2$ ;  $\blacktriangle$ ,  $\Delta x^+ \approx 3.2$ ,  $\Delta z^+ \approx 1.6$ ;  $\nabla$ ,  $\Delta x^+ \approx 2.2$ ,  $\Delta z^+ \approx 1.1$ .

follow the convention introduced by Seo *et al.* (2013) and introduce the Weber number,  $We^+ = \rho u_\tau \nu / \sigma$ , where  $\sigma$  represents the surface tension. We should note that the Weber number that is naturally relevant to interface breakage should involve  $L^+$  and slip velocity (which is not known *a priori*). However, the adopted  $We^+$  makes the subsequent scaling analysis of interface deformation easier since it remains unchanged when we change the texture size,  $L^+$ .

In this study, we consider values for  $We^+$  corresponding to practical applications. For a water density of  $1000 \text{ kg/m}^3$ , a surface tension of  $0.073 \text{ N/m}$ , a typical boundary layer velocity of  $U_\infty = 6 - 10 \text{ m/s}$  over a plate  $0.5\text{-}10 \text{ m}$  long, the values would be in the range  $We^+ = 10^{-3} - 10^{-2}$ .

### 3. Numerical method

The three-dimensional Navier-Stokes equations are discretized and solved computationally with the code of Bose *et al.* (2010), adapted to treat DNS of superhydrophobic textured boundaries. The code uses a second-order finite-difference scheme on a staggered mesh (Morinishi *et al.* 1998). The grid is Cartesian with uniform spacing in the streamwise ( $x$ ) and spanwise ( $z$ ) directions, and stretching in the wall-normal ( $y$ ) direction. The time discretization uses a second-order Adams-Bashforth scheme for the non-linear and wall-parallel diffusion terms, and a second-order Crank-Nicholson scheme for the wall-normal diffusion terms. Incompressibility is imposed through a fractional step implementation (Kim & Moin 1985). The computational domain is a periodic channel of ratio length–width–height of  $2\pi \times \pi \times 2$ , standard for simulations that focus on near-wall effects (Martell *et al.* 2009, 2010; García-Mayoral & Jiménez 2012). The flow is driven by a time-constant mean pressure gradient, so that  $Re_\tau$  is fixed. The main set of simulations is conducted at  $Re_\tau \approx 200$ , with two simulations at  $Re_\tau \approx 400$  to investigate Reynolds-number effects.

The time integration is conducted using a constant Courant-Friedrichs-Lewy number,  $CFL = 0.25$ , so that the variable time step is determined by

$$\Delta t = CFL \times \left( \max \left\{ \frac{|u|}{2\Delta x} + \frac{|v|}{2\Delta y} + \frac{|w|}{2\Delta z} + \frac{4}{Re\Delta x^2} + \frac{4}{Re\Delta z^2} \right\} \right)^{-1}. \quad (3.1)$$

The simulations were run for at least 35 largest-eddy-turnover times  $\delta/u_\tau$ , of which the first 10 were discarded for statistical sampling, to avoid any contamination from initial transients.

Case	Surface type	$L^+$	$Re_\tau$	$D_x^+$	$D_z^+$	$N_x \times N_z \times N_y$
S	Smooth	n.a.	197.5	1240.9	620.5	$192 \times 192 \times 128$
$S_{Re}$	Smooth	n.a.	395.0	2481.9	1240.9	$256 \times 256 \times 256$
P6	Posts	6.46	197.5	1240.9	620.5	$2304 \times 1152 \times 128$
P13	Posts	12.93	197.5	1240.9	620.5	$1152 \times 576 \times 128$
P26	Posts	25.85	197.5	1240.9	620.5	$1152 \times 576 \times 128$
P39	Posts	38.78	197.5	1240.9	620.5	$576 \times 288 \times 128$
P78	Posts	77.56	197.5	1240.9	620.5	$384 \times 192 \times 128$
P155	Posts	155.1	197.5	1240.9	620.5	$192 \times 192 \times 128$
$P155_{Re}$	Posts	155.1	395.0	2481.9	1240.9	$384 \times 384 \times 192$
R155	Ridges	155.1	197.5	1240.9	620.5	$192 \times 192 \times 128$

TABLE 1. Simulation parameters.  $L^+$  is the pattern spacing, and  $Re_\tau$  is the friction Reynolds-number. Domain size for streamwise and spanwise direction is  $D_x^+$  and  $D_z^+$ . The spatial resolution is given by  $N_x$ ,  $N_z$ , and  $N_y$ , the number of grid points for streamwise, spanwise, and wall-normal direction.

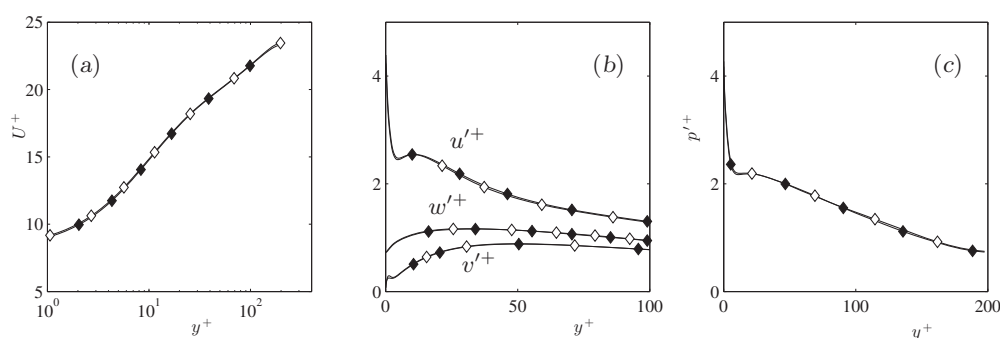


FIGURE 4. Resolution test for the post geometry with  $L^+ \approx 26$  at  $Re_\tau \approx 200$ . (a) Mean streamwise velocity profile; (b) velocity rms fluctuations; (c) pressure rms fluctuations. ;  $\diamond$ ,  $\Delta x^+ = \Delta z^+ \approx 2.2$ ;  $\blacklozenge$ ,  $\Delta x^+ = \Delta z^+ \approx 1.1$ .

All simulations use symmetric channels, with both walls being either smooth or superhydrophobic. In the latter case, the gas-liquid interface is modeled as a perfect-slip boundary condition, resulting in a pattern of slip and no-slip conditions (Martell *et al.* 2009). We study the patterns sketched in figures 1(a), streamwise-aligned ridges, and 1(b), posts distributed uniformly in the streamwise ( $x$ ) and spanwise ( $z$ ) directions. Spanwise-aligned ridges are less efficient for drag reduction than streamwise-aligned ones (Min & Kim 2004; Martell *et al.* 2009; Choi *et al.* 2006), and thus we have not considered them in our study. The pattern thickness is set to  $W = L/3$ , so the solid fraction is  $1/9$  for posts and  $1/3$  for ridges.

In the wall-normal direction, the stretched grid has  $\min(\Delta y^+) = 0.15$  at the wall and  $\max(\Delta y^+) = 12$  at the center of the channel. The  $x$  and  $z$  spatial resolution is determined by the texture size, so that the number of points per texture unit  $n_x$ ,  $n_z$  is sufficient to resolve the mean texture properties (e.g.  $U_s^+$ ,  $p_{rms,y=0}^+$ ). The parameters of the simulations are summarized in Table 1. Even for the largest textures, this resolution is finer than that required for DNS of turbulence, with  $\Delta x^+ = 6.4$ ,  $\Delta z^+ = 3.2$  at most. However, detailed pressure distributions near posts need further attention, due to the singularity at the post edge facing the streamwise slipping flow, where the patterned slip/no-slip boundary condition is analogous to the boundary layer over a sharp corner

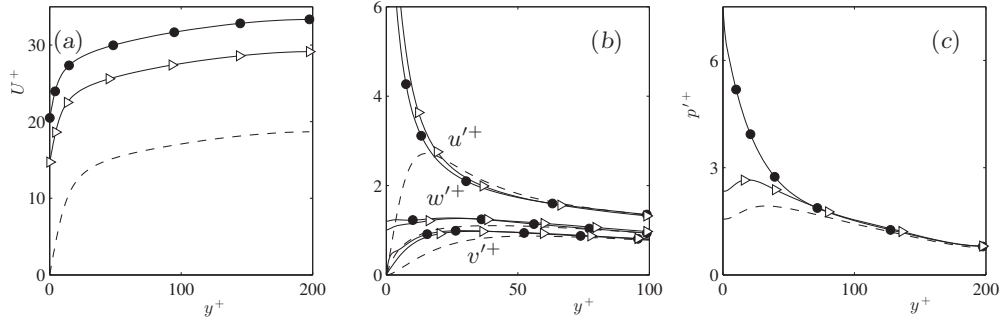


FIGURE 5. Comparison of statistics for  $L^+ \approx 155$  at  $Re_\tau \approx 200$ . (a) Mean streamwise velocity profile; (b) velocity rms fluctuations; (c) pressure rms fluctuations.  $\bullet$ , P155, post;  $\blacktriangleright$ , R155, streamwise ridge; ----, smooth walls.

(Van Dyke 1962). This singularity gives rise to resolution-dependent values of the pressure at the edge. Nevertheless, given the nature of equation (2.3), and the pinned boundary condition for air-water interface, the corner singularity still leads to regular solution for the interface deformation. As a result, we have been able to establish grid converged results for interface and pressure fields away from corners with the adopted resolutions.

The code was validated with the turbulent, smooth-wall channel at  $Re_\tau \approx 395$  of Moser *et al.* (1998), and the superhydrophobic channels with streamwise ridges of gas fraction 1/2 and size  $L^+ \approx 74$  and 148, also at  $Re_\tau \approx 395$ , from Martell *et al.* (2010). Resolution tests were run for case P155 with  $n_x = 48$ ,  $n_z = 96$  and  $n_x = 72$ ,  $n_z = 144$ , and results showed grid convergence, as shown in figure 3. To assess the validity of the grid resolution in the small-texture limit, a resolution test for P26 was also run at  $n_x = n_z = 12$ , and the two grid resolutions also make excellent agreement, as shown in figure 4. The mean slip velocity of P155 has error of the coarsest case to the finest case below 1%, and all other cases had smaller convergence error.

We have also performed a domain-size convergence study to ensure that the presented statistics are not affected by the computational domain size. To guide the selection of domain sizes for this study, we have analyzed correlation statistics in both streamwise and spanwise directions at various distances from the wall. Details of this study are presented in Appendix A.

## 4. Results and discussion

### 4.1. Geometry effects on pressure characteristics

First we compare the surface geometries of posts and streamwise ridges focusing on their difference in pressure characteristics with fixed  $L^+$ . With equal  $W/L$ , both surfaces have similar mean and rms velocities, as shown in figure 5. While their turbulence intensities have no notable difference, the pressure fluctuations for posts are considerably higher. This contrast can be well explained by the detailed pressure contours at  $y^+ = 0$ , shown for a particular instant in figure 6.

As schematically shown in figure 7, the slipping flow is diverted by the posts when it travels downstream, and a stagnation region with high pressure is formed immediately upstream of every post. This comparison is rather qualitative in the large wavelength limit,  $L^+ \approx 155$ , but we will show later that the stagnation pressure is mainly a function of  $L^+$  –through its dependence on  $U_s^+$ , whereas the pressure fluctuations for streamwise ridges are less sensitive to the changes in slip or texture size.

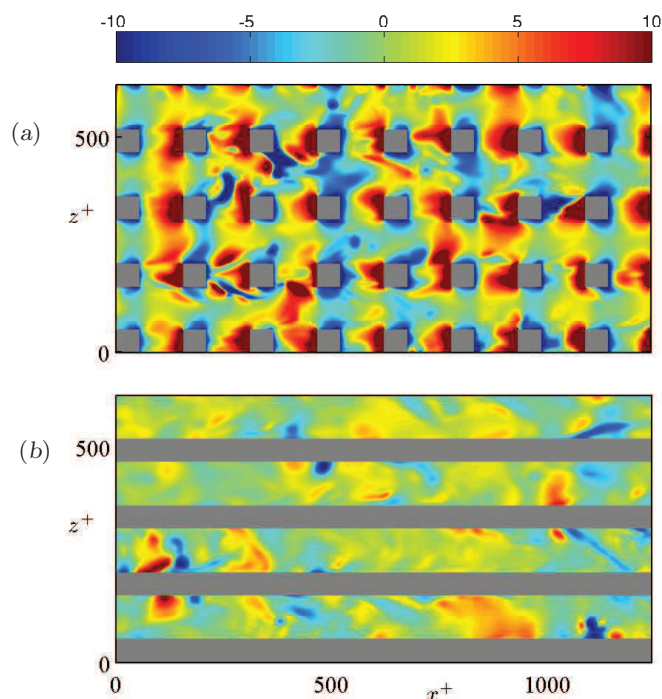


FIGURE 6. Comparison of instantaneous pressure contours,  $p^+ = p/(\rho u_\tau^2)$ , at  $y^+ = 0$ , for cases with  $Re_\tau \approx 200$  and  $L^+ \approx 155$ . From blue to red, the fluctuations range between  $-10$  and  $10$  wall units. (a) P155, (b) R155

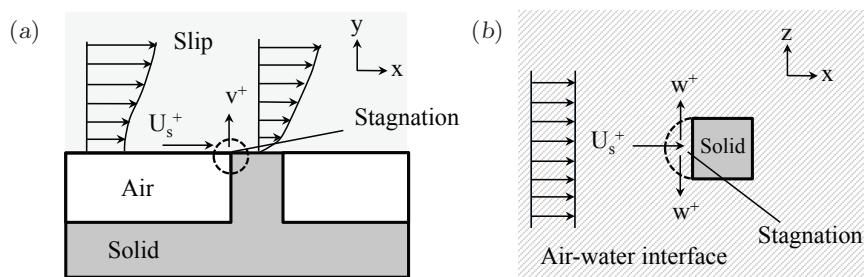


FIGURE 7. Schematic representation of stagnation phenomenon in (a) streamwise/wall-normal, (b) wall parallel plane at  $y^+ = 0$ .

#### 4.2. Reynolds-number effect

Before discussing the effect of  $L^+$ , it is worth briefly discussing the effect of a given texture with fixed  $L^+$  at different  $Re_\tau$ . According to the classical theory of wall turbulence, surface manipulations act only on the innermost region of the turbulent flow. From the point of view of the outer flow and its bulk properties, they only modify the intercept of the logarithmic velocity profile (Clauser 1956), in turn shifting the free stream velocity and changing the friction coefficient. For the above statement to hold, however, the perturbations induced by the surface should only penetrate a small portion of the boundary layer (Jiménez 2004). The depth of the penetration can be expected to scale with the typical length of the surface manipulations, in our case  $L^+$ . A condition for the surface not to perturb the whole flow thickness would then be  $L^+ \ll Re_\tau$ . This condition was

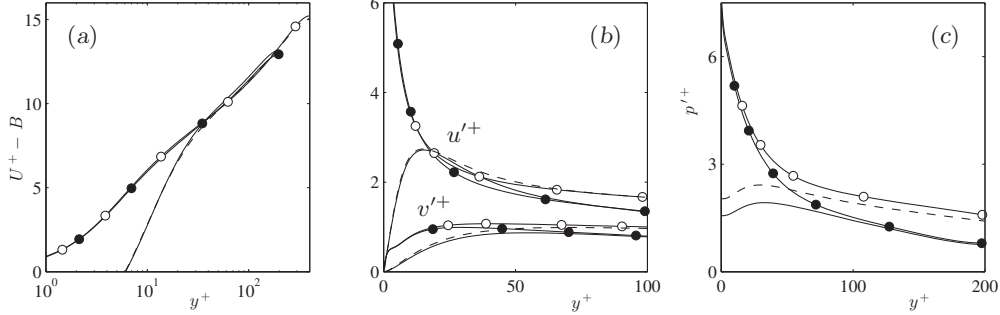


FIGURE 8. Comparison of statistics for post geometries with  $L^+ \approx 155$  at  $Re_\tau \approx 200$  and  $Re_\tau \approx 400$ . (a) Mean streamwise velocity profile; (b) velocity rms fluctuations; (c) pressure rms fluctuations. The intercept  $B$  of the logarithmic region in the  $U^+$  profile has been subtracted in (a) for better comparison of the outer region.  $\bullet$ ,  $Re_\tau \approx 200$ , posts;  $\text{—}$ ,  $Re_\tau \approx 200$ , smooth walls;  $\circ$ ,  $Re_\tau \approx 400$ , posts;  $\text{---}$ ,  $Re_\tau \approx 400$ , smooth walls.

analyzed for riblets, another drag-reducing surface, in García-Mayoral & Jiménez (2012), finding that in that case  $L^+ \approx 0.2Re_\tau$  was a sufficient condition. For our superhydrophobic posts at  $Re_\tau \approx 200$ , that condition would clearly not be met by the cases of larger  $L^+$ . Therefore, we have simulated the most critical case  $L^+ \approx 155$  also at  $Re_\tau \approx 400$ . The results, of which some statistics are portrayed in figure 8, show that the influence of the texture extends only up to  $y^+ \approx 50\text{--}80$ . In the core for the channel, the flow behaves like that over smooth walls, albeit with a shifted velocity profile. Near the wall, the effect of the texture is essentially independent of the Reynolds number.

These results provide confidence in the relevance of our investigation to practical flows in which Reynolds number is higher. In other words, flow modifications by superhydrophobic surfaces are confined to the near wall region, and are primarily controlled by  $L^+$  and  $We^+$ .

Note that the pressure fluctuations at the wall for smooth channels increase logarithmically with  $Re_\tau$ , yet they do not reach values larger than  $p'_{\text{rms}} \approx 3$  even at  $Re_\tau \approx 4000$  (Hoyas & Jiménez 2006; Lozano-Durán & Jiménez 2014). These are much smaller than the stagnation pressures reported here.

### 4.3. Turbulence statistics

The slip velocity, mean velocity profile, turbulent intensities, and pressure fluctuations for  $L^+ \approx 6 - 155$  are summarized in figure 9. Up to  $L^+ \approx 10$ , the effect of  $L^+$  on the slip velocity follows a linear relationship, as shown in figure 9(a), and as predicted by the semi-analytical formula of Ybert *et al.* (2007) and by our laminar flow simulation with the same texture layout,

$$U_s^+ = C_Y L^+, \quad (4.1)$$

where  $C_Y = 0.535$ , for a solid fraction,  $\phi = 1/9$ .  $U_s$  can also be expressed in terms of a slip length,  $b$ , so that in wall-unit scaling  $U_s^+ = b^+$ . The linear relationship of equation (4.1) breaks when the surface wavelength becomes  $L^+ \gtrsim 10$ . Deviation from linear slip theory is expected since the theory is based on Stokes' flow equations, which loses its accuracy as the Reynolds number based on texture size becomes large. Our results show for the first time  $U_s^+$  versus  $L^+$  covering the entire range from linear regime to fully nonlinear large  $L^+$  limit, for a three-dimensional superhydrophobic texture. Previous results have shown similar behavior for two-dimensional streamwise ridges, covering  $L^+$  values down to Park *et al.* (2013) and Türk *et al.* (2014).

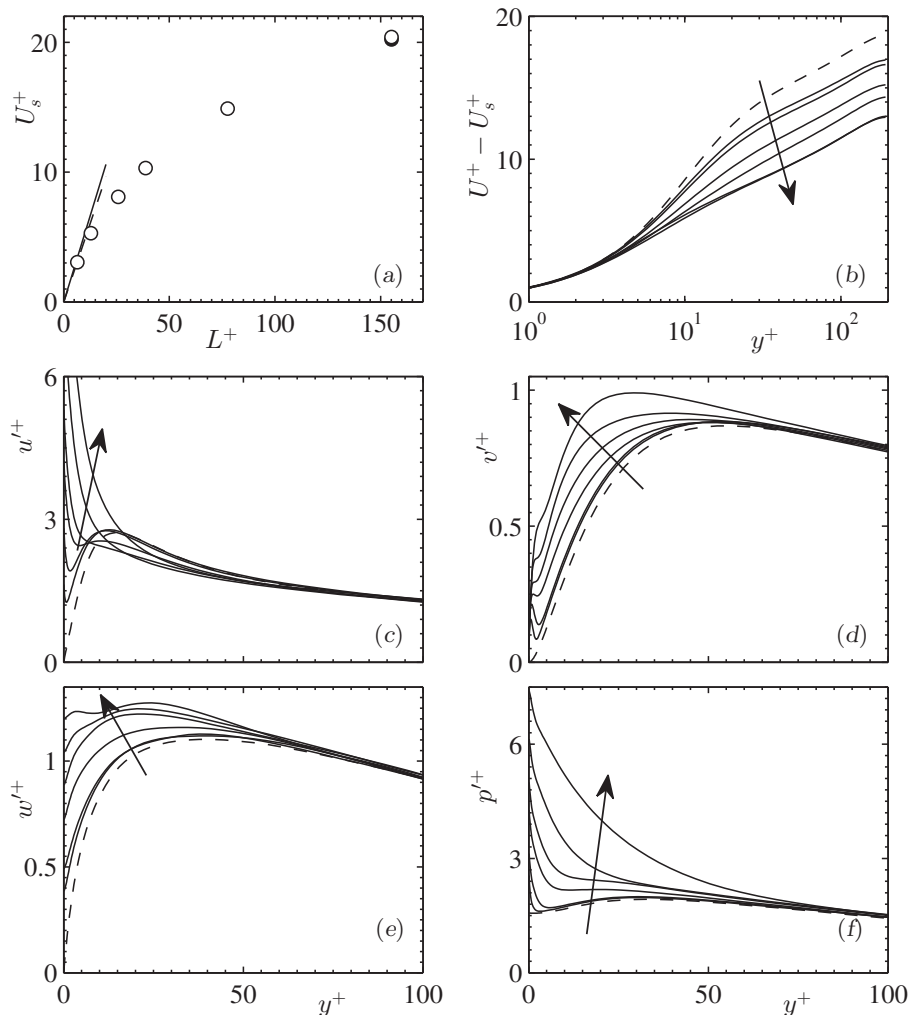


FIGURE 9. Comparison of superhydrophobic posts for different  $L^+$  at fixed  $Re_\tau \approx 200$ , with arrows indicating increasing  $L^+$ . (a) Slip velocity. The solid line indicates the theoretical prediction of Ybert *et al.* (2007), the dashed line is the prediction from a laminar simulation with the same texture layout. The result for  $L^+ \approx 155$  and  $Re_\tau \approx 400$  is included for reference with a solid symbol. (b) Mean velocity profile, with the slip subtracted. (c), (d) and (e), streamwise, wall-normal and spanwise velocity rms fluctuations. (f) pressure rms fluctuation. ----, smooth channel; —, superhydrophobic posts.

Given that the large values of  $U_s^+$  in our simulations can become comparable with the bulk and centerline velocities, they can obscure some of the effects of the surface on the velocity profile. For this reason, figure 9(b) compares the profiles offset by their respective slips,  $U - U_s^+$ . The profiles show a behavior similar to that of conventional roughness, for which the logarithmic region is increasingly extended towards the wall as the roughness size, or  $L^+$  in our case, increases. The logarithmic region of the profile is given by

$$U^+ - U_s^+ = \frac{1}{\kappa} \log(y^+) + B, \quad (4.2)$$

where  $\kappa$  is Kármán constant and  $B$  is the intercept of the logarithmic profile. As  $L^+$

increases,  $B$  decreases from its smooth-wall value  $B \approx 5$ , and seems to reach asymptotically  $B \approx 0$  for  $L^+ \gtrsim 70$ . The decrease in  $B$  through surface manipulations implies an increase in friction, which has been discussed and quantified thoroughly in the literature (Jiménez 1994; Luchini 1996; Spalart & McLean 2011; García-Mayoral & Jiménez 2011*a*). In the case of superhydrophobic surfaces, this deleterious effect is largely offset by the drag-reducing increase in  $U_s^+$ . More interestingly, we note that for textures large enough,  $L^+ \gtrsim 70$ , the typical velocity profile in the viscous and buffer layers is completely destroyed, except for two wall units above the surface, and that the logarithmic profile seems to extend to the immediate vicinity of the wall. This suggests that, even if the surface remains flat, the distortion introduced by the alternating slip/no-slip conditions can completely disrupt the near-wall cycle, as conventional rough surfaces do (Jiménez 2004).

Figure 9 also shows how the fluctuations intensify as  $L^+$  increases. Those induced by the texture grow with the pattern wavelength, and the impact is most significant on the streamwise and pressure statistics. The large values of  $u'$  are essentially due to the large variations of  $u$  between regions over the free-slip interface, where  $u^+ \approx 20$ , and the regions over the no-slip obstacles, where  $u^+ \approx 0$ . As the distribution of  $u$  depends essentially on the  $x$ - $z$  position, the values fluctuate rather in space than in time. The wall-normal and spanwise velocity fluctuations do not experience such large surface effects, even though finite perturbations are still observable near the surface. A homogeneous slip length model (Min & Kim 2004; Busse & Sandham 2012) is not able to capture this trend, since it homogenizes the spatial variation of the velocity at the boundary.

The pressure fluctuations deserve special attention since they can be responsible for the breakup of the interface, and are analyzed independently in §4.5. The rms values exhibit dramatic increases near the wall, as  $L^+$  increases, similar to those of  $u'$ . Note that this would not be the case for perfectly aligned ridges, such as those shown in figure 5(c).

In all of the profiles investigated, the effect of the texture layout decays rapidly with  $y^+$ , and even for the larger  $L^+ \approx 150$  it does not extend beyond  $y^+ \approx 60$ . This extension of the distortion of the fluctuations across the full buffer layer is likely connected to the disruption of the near-wall cycle mentioned above. For textures of realistic size, though, and up to  $L^+ \approx 15$ , their presence only affects the rms values in small near-wall kinks confined within the viscous sublayer,  $y^+ \lesssim 5$ .

#### 4.4. Decomposition of fluctuations

To better understand the statistical data, instantaneous distributions of the wall-normal vorticity and the pressure on the superhydrophobic surface are portrayed in figures 10 and 11 (movies available in the online supplementary material). At small  $L^+$ , the distribution of  $\omega_y^+$  is dominated by the footprint of near-wall turbulent streaks, with the exception of the small-scale shedding of flow from the posts. This shedding becomes however increasingly important as  $L^+$  increases, and becomes dominant for  $L^+ \gtrsim 35$ .

Two distinct contributions can also be observed in the instantaneous pressure fluctuations near the wall as shown in figure 11. The first is the footprint of turbulent pressure fluctuations as they are advected downstream, with typical lengthscales  $\sim 100\nu/u_\tau$ , and similar to those observed over smooth walls. The second is a stationary distribution caused by the stagnation of flow in front of and behind the posts. Again, the former dominates for small textures, and the latter for large ones.

To analyze separately the contributions due to the overlying turbulence and that due to the surface texturing, for any variable  $q$  we decompose its fluctuations  $q'$  into a spatially-

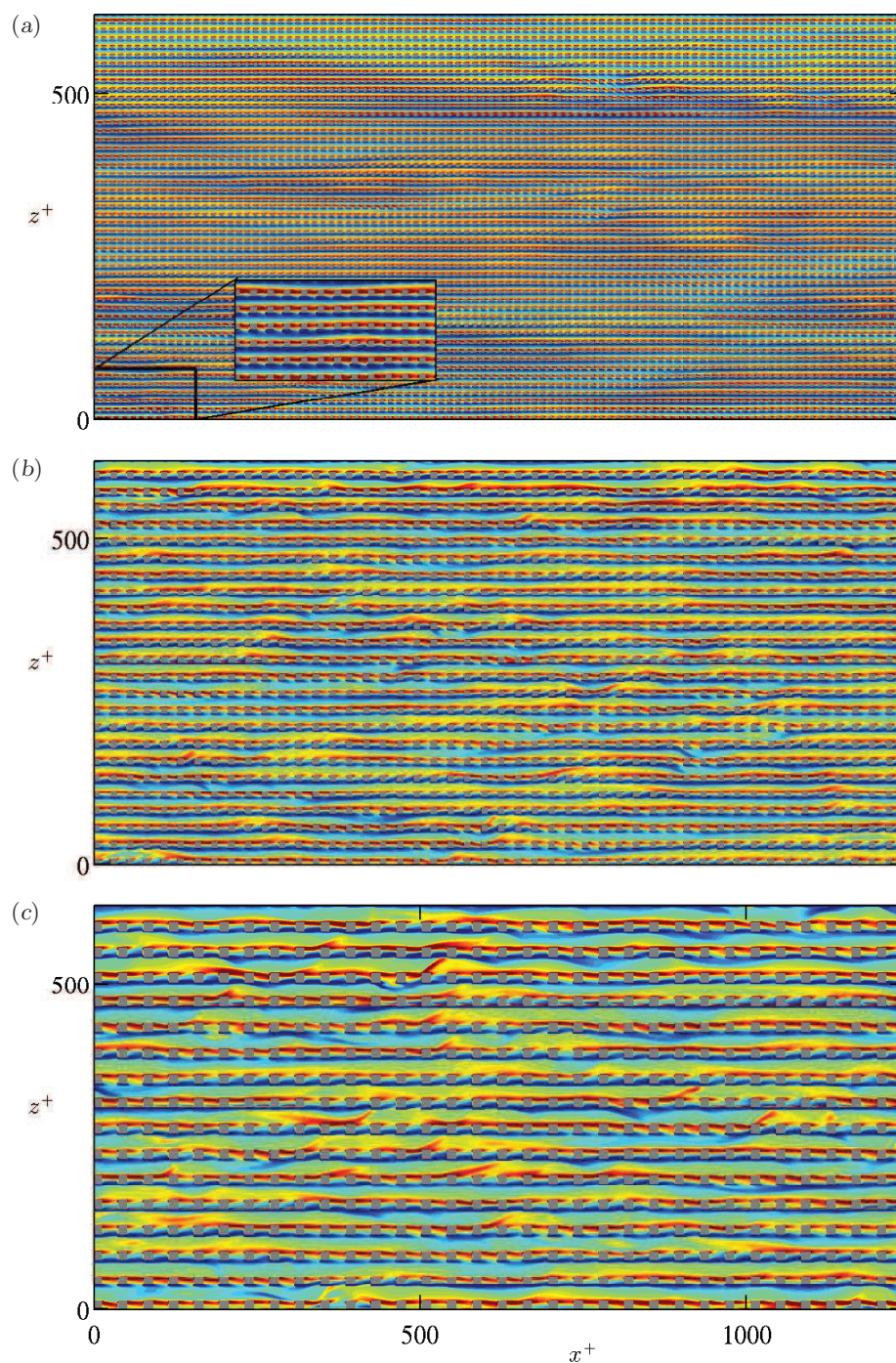


FIGURE 10. Comparison of instantaneous wall-normal vorticity,  $\omega_y^+$ , contours at  $y = 0$ , for cases (a) P13, (b) P26, and (c) P39. From blue to red, the fluctuations range between  $-1.2$  and  $1.2$  wall units. The rectangular inset in (a) is a magnification of the boxed region in the main plot.

14

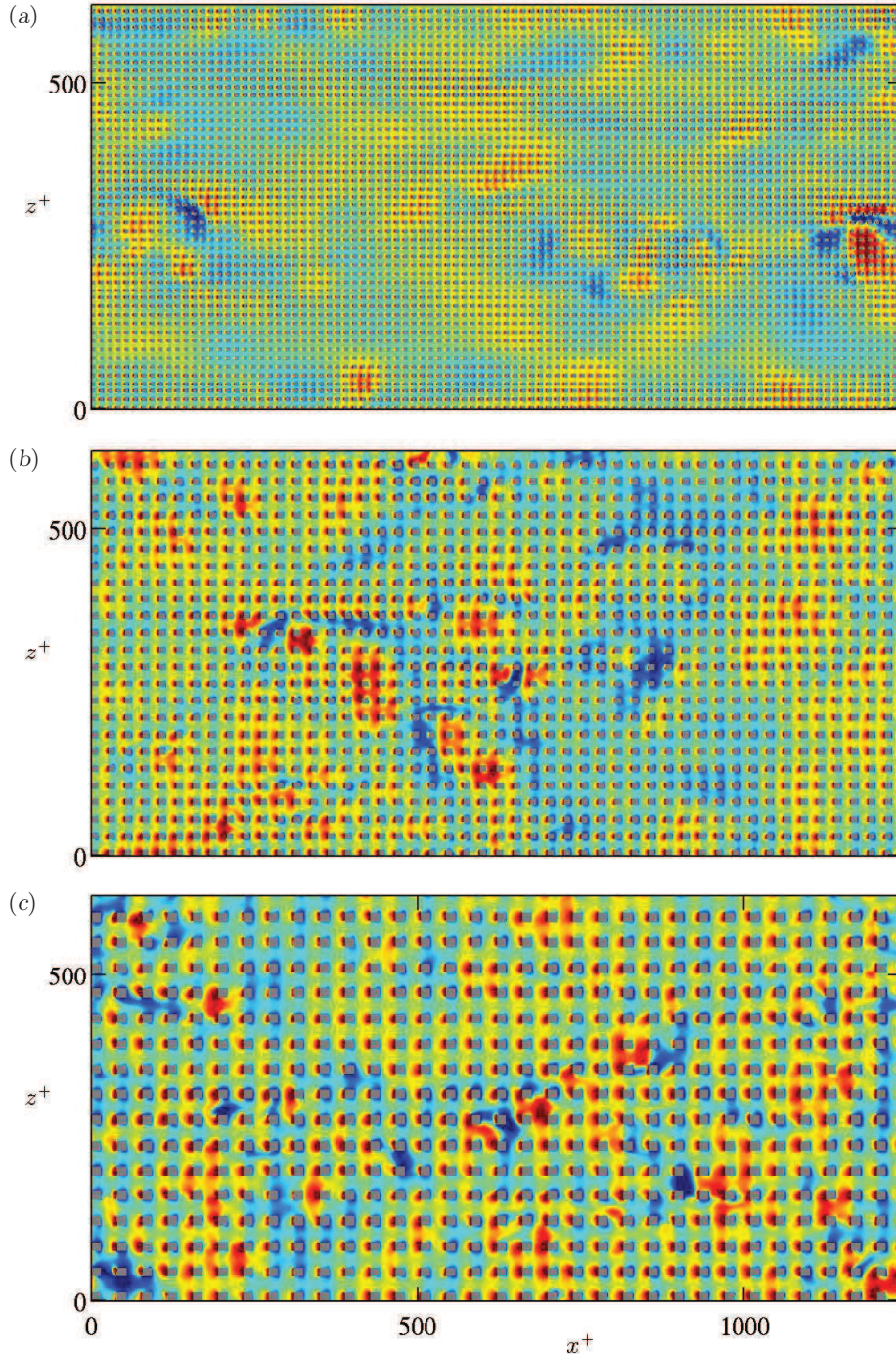
*J. Seo, R. García-Mayoral and A. Mani*

FIGURE 11. Comparison of instantaneous pressure contours,  $p^+$ , at  $y=0$ , for cases (a) P13, (b) P26, and (c) P39. From blue to red, the fluctuations range between  $-10$  and  $10$  wall units.

coherent component  $\tilde{q}$ , which is time-independent, and a random component  $q''$ , so that

$$q(x, z, y, t) = \bar{q}(y) + q'(x, z, y, t) = \bar{q}(y) + \tilde{q}(\tilde{x}, \tilde{z}, y) + q''(x, z, y, t), \quad (4.3)$$

where  $\tilde{x} = \text{modulo}(x, L_x)$  and  $\tilde{z} = \text{modulo}(z, L_z)$  are the relative streamwise and spanwise coordinates within each pattern periodic unit, and where the coherent component  $\tilde{q}$  is averaged over time and over the number of periodic units. This type of decomposition, into ‘coherent’ and ‘random’ components, was introduced by Reynolds & Hussain (1972), and has been extensively used to analyze turbulent flows over complex surfaces (Choi *et al.* 1993; Jiménez *et al.* 2001; García-Mayoral & Jiménez 2011*b*; Jelly *et al.* 2014; Türk *et al.* 2014).

The result of applying this decomposition to the velocity and pressure fluctuations is illustrated in figure 12. The figure shows for instance that most of the previously observed change in  $u'$  when computing the raw rms is due to the coherent distribution  $\tilde{u}$ , while the turbulent component  $u''$  remains essentially unaltered at magnitudes similar to those in a smooth wall case. In all quantities plotted, the turbulent component of the fluctuations is augmented with increasing texture size, but the augmentation is rather modest and confined to the near wall ( $y^+ \lesssim 60$ ).

As discussed in §4.2, the effect of the surface is essentially Reynolds-number independent, and the coherent contribution remains roughly constant as shown in the figure 12 for  $Re_\tau \approx 200$  and  $Re_\tau \approx 400$ .

As  $L^+$  increases, the coherent component of the pressure increases dramatically, while the random contribution remains close to that of smooth channels. This dramatic increase of  $\tilde{p}^+$  with  $L^+$  sets a limit to the pattern size for practical applications, since the high stagnation pressures are bound to deform and eventually break-up the entrapped air bubbles.

#### 4.5. Scaling and self-similarity of stagnation pressure

In the limit of vanishing spacing,  $L^+ \rightarrow 0$ , the flow in the vicinity of the texture is dominated by viscous effects and can be analyzed as a Stokes flow (Luchini *et al.* 1991). In that regime, dimensional analysis predicts that  $\tilde{p}^+ \sim 1$  is independent of  $U_s^+$ . Conversely, for  $L^+ \rightarrow \infty$ , inertial effects are dominant and dimensional analysis predicts  $\tilde{p} \sim U_s^{+2}$ . To check the actual scaling observed in our DNSs, we first focus on the values of  $\tilde{p}^+$  at  $y^+ = 0$ ,  $\tilde{p}_0^+$ , shown in figure 13(a). The value for  $L^+ \approx 6$  is very close to that predicted for  $L^+ \rightarrow 0$  from a viscous, laminar simulation. However, from there on  $\tilde{p}_0^+$  seems to exhibit a linear scaling with  $U_s^+$ , which is close to

$$\tilde{p}_{0,\text{rms}}^+ = 0.28U_s^+ + 1.26. \quad (4.4)$$

This behavior is intermediate to those predicted for  $L^+ \rightarrow 0$  and  $L^+ \rightarrow \infty$ .

The coherent pressure  $\tilde{p}^+$  also exhibits a self-similar behavior when its variation with  $y^+$  is considered. Figure 13(b) shows that  $\tilde{p}_{\text{rms}}^+(y^+, L^+)$  satisfies a self-similar scaling that can be expressed as

$$\tilde{p}_{\text{rms}}^+ \sim \exp\left(-\frac{2\pi}{L^+}y^+\right). \quad (4.5)$$

The exponential decay in  $y^+$  is reminiscent of a solution to the Laplace equation with periodic behavior in the wall-tangential direction with period  $L^+$ . Such a solution is consistent with solutions over patterned surfaces in the Stokes’ flow limit (Belyaev & Vinogradova 2010; Kamrin *et al.* 2010). However, it is remarkable that the same scaling still holds in the turbulent flow regimes for  $L^+$  values as high as order hundred.

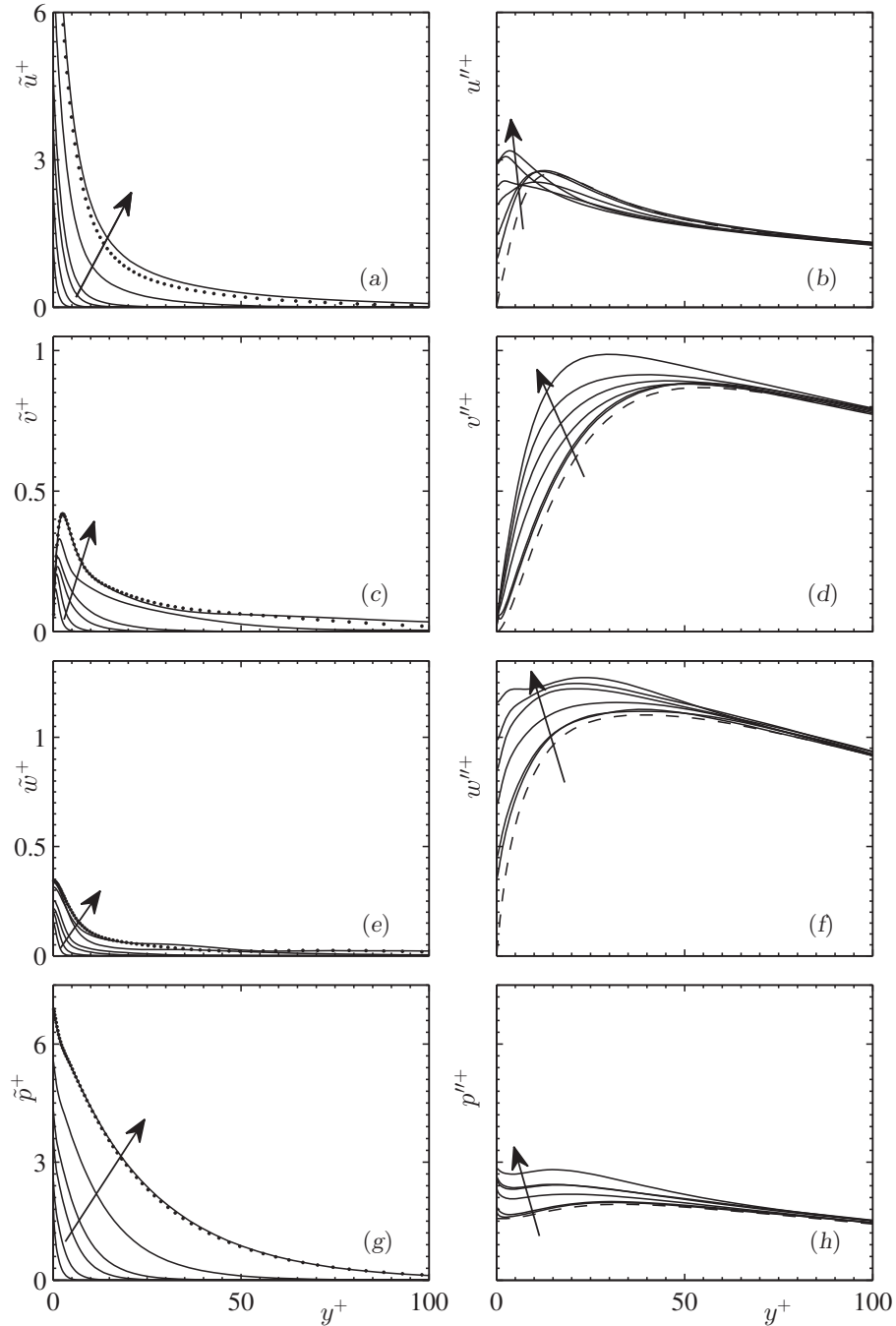


FIGURE 12. Decomposition of fluctuation statistics for different  $L^+$  at fixed  $\text{Re}_\tau \approx 200$ , with arrows indicating increasing  $L^+$ . (a)  $\tilde{u}_{\text{rms}}^+$ , (b)  $u''_{\text{rms}}^+$ , (c)  $\tilde{v}_{\text{rms}}^+$ , (d)  $v''_{\text{rms}}^+$ , (e)  $\tilde{w}_{\text{rms}}^+$ , (f)  $w''_{\text{rms}}^+$ , (g)  $\tilde{p}_{\text{rms}}^+$ , (h)  $p''_{\text{rms}}^+$ , ----, smooth channel; —, superhydrophobic posts, ·····, superhydrophobic posts,  $\text{Re}_\tau \approx 400$ ,  $L^+ \approx 155$ .

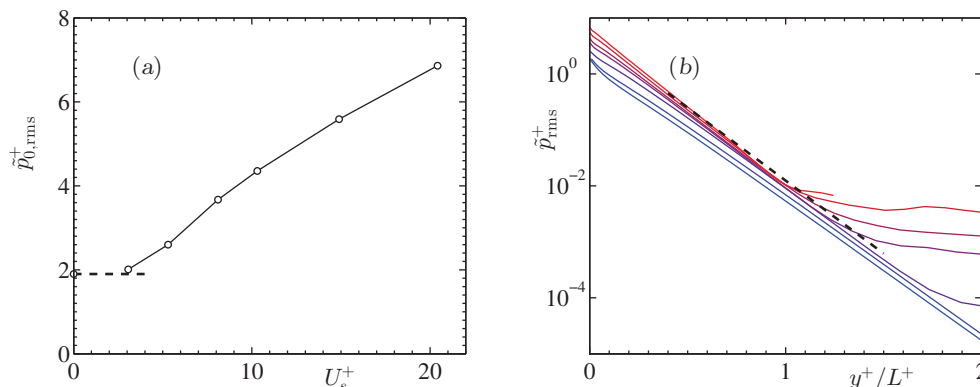


FIGURE 13. (a) Coherent pressure fluctuation values at  $y^+ = 0$ , with the dashed line marking the asymptotic limit for a laminar solution at  $L^+ \rightarrow 0$ . (b) Self similar behavior of the rms of the stagnation contribution to the pressure,  $\tilde{p}(y)$ . From blue to red, increasing  $L^+$  from  $L^+ \rightarrow 0$  to  $L^+ \approx 155$ . The dashed line indicates  $\tilde{p}^+ \sim \exp(-6y^+/L^+)$ .

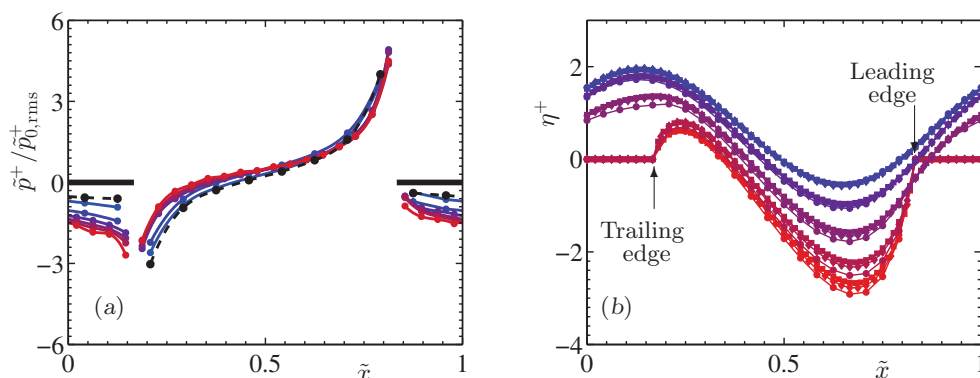


FIGURE 14. (a) Streamwise distribution of  $\tilde{p}$  at  $y^+ = 0$  for the  $\tilde{x}$ -line running through the middle of the posts. Each case has been scaled with its in-plane rms value. From blue to red,  $L^+$  increases from  $L^+ \approx 6$  to  $L^+ \approx 155$ . The black dashed lines correspond to the laminar solution for  $L^+ \rightarrow 0$ . The black solid lines mark the location of the post. Each points are interpolated with spline. (b) Interface deformation,  $\eta^+$  at  $L^+ \approx 155$ ,  $Re_\tau \approx 200$ , and  $We^+ = 10^{-3}$ . From blue to red, each lines are plotted in evenly spaced spanwise locations, and the red ones are on plane where the posts locate.  $\bullet$ ,  $\Delta x^+ \approx 6.4$ ,  $\Delta z^+ \approx 3.2$ ;  $\blacklozenge$ ,  $\Delta x^+ \approx 3.2$ ,  $\Delta z^+ \approx 1.6$ ;  $\blacksquare$ ,  $\Delta x^+ \approx 2.2$ ,  $\Delta z^+ \approx 1.1$

Self similarity is not only observed in the rms value of  $\tilde{p}$ , but also in its  $\tilde{x}$ - $\tilde{z}$  spatial distribution, as shown in figure 14(a) for  $\tilde{p}_0^+$ .

#### 4.6. Interface deformation

The analysis of the pressure is interesting in itself, but for practical applications it is even more interesting to analyze how that pressure would deform the interface. An additional advantage is that, while the pressure fields are singular at the solid/interface edges, the deformation fields are not, and are therefore less sensitive to the grid resolution. Interface deformation can be obtained from the stagnation pressure using equation (2.3).

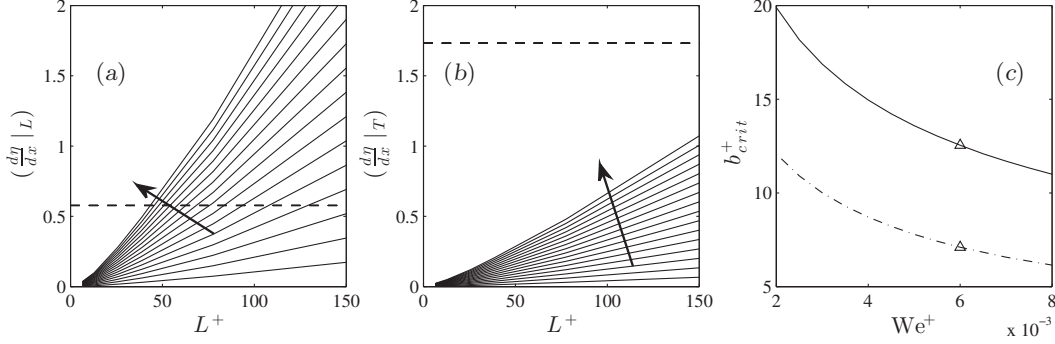


FIGURE 15. Interface slope at the post edge as a function of  $L^+$ , for different  $We^+$  ranging from  $5 \times 10^{-4}$  to  $8 \times 10^{-3}$  with successive interval of  $5 \times 10^{-4}$  at (a) the leading and (b) trailing edge. Arrows indicate increasing  $We^+$ . The black dashed line represents  $\theta_L = 120$  degrees in (a) and  $\theta_T = 120$  degree in (b). The intersection of dashed line with a solid line represents the critical  $L^+$  for the corresponding  $We^+$ . For each critical point, the resulting slip length is plotted as a function of  $We^+$  in (c). The dashed-dot line represents same calculation for a material with critical contact angle of 100 degree. The triangle symbol indicate a typical  $We^+$  corresponding to  $U_\infty = 10\text{m/s}$ .

The contact angle is defined at trailing and leading edges of the posts as

$$\theta_L = \frac{\pi}{2} + \tan^{-1} \left( \left. \frac{d\eta}{dx} \right|_L \right), \quad (4.6)$$

$$\theta_T = \pi - \tan^{-1} \left( \left. \frac{d\eta}{dx} \right|_T \right), \quad (4.7)$$

as portrayed in figure 2(b). The interface slope,  $\frac{d\eta}{dx}$ , is measured from the spline interpolation at the contact point. The interface is deflected down in stagnation pressure regions, and the maximum interface slope occurs at the mid point of the posts leading edge, as shown in figure 14(b). One possible failure scenario is related with this maximum deformation, with its onset determined by  $\theta_L$  becoming equal to the microscopic advancing contact angle,  $\theta_{adv}$ . At this onset the air-water interface will not remain pinned at the edge of the post and will start moving down till further wetting the post. We consider this condition as the onset of failure of the SHS surface. Similar failure mechanism would pertain when  $\theta_T$  becomes equal to the microscopic receding contact angle,  $\theta_{rec}$ .

This procedure allows us to establish a criterion to estimate a critical  $L^+$  for stable drag reduction as a function of  $We^+$ . We note that the linear Young-Laplace equation, as shown in equation (2.3), is only valid for small deformations, where  $d\eta/dx \ll 1$ . However, to obtain only a rough estimate of onset interface breakage, we here resort to linear solutions. Additionally we assume a representative microscopic advancing contact angle  $\theta_{adv} = 120$  degrees (equivalent of  $d\eta/dx = 0.58$ ), consistent with best hydrophobic materials. Note that the apparent macroscopic contact angle, which is typically closer to 180 degrees for a textured material, is not the relevant parameter in this sub-texture analysis.

Figure 15(a) shows the computed interface slope at the pinned location as a function of  $L^+$  for different values of  $We^+$ . For each  $We^+$  as one increases the  $L^+$  (e.g., experimentally by increasing the texture size, for fixed channel height, pressure gradient, and fluid properties) the critical slope will be reached at some critical value of texture size,  $L_{crit}^+$ . Figure 15(b) shows the same for the slope at the trailing edge of the post, indicating that the leading edge slope is more critical to failure. Figure 15(c) summarizes these results

by showing the critical values as a function of  $We^+$ . Here, we have used values of  $U_s^+$  from figure 9(a) and have directly reported the bounds on achievable slip length.

As  $We^+$  increases,  $L_{crit}^+$ , and thus achievable slip length decreases, suggesting an upper bound for practical applications. Proper nondimensionalization of the Young-Laplace equation together with equation (4.4), suggest the following scaling relation for the onset of interface breakage:

$$We^+ U_s^+ L^+ = O(1) \quad (4.8)$$

where the order one constant at the right hand side depends on the advancing contact angle. Remarkably same relation would hold in the limit of nonlinear Young-Laplace for large deformations; only the right hand-side constant would be different.

The results shown in figure 15(c) have significance in practical applications and in design of superhydrophobic surfaces. We note that the defined  $We^+ = \rho u_\tau \nu / \sigma$  is mostly controlled by the freestream velocity and only has logarithmic dependence on the boundary layer thickness in turbulent flows (Lozano-Durán & Jiménez 2014). For practical purposes  $u_\tau$  can be estimated to be between 20 to 30 times smaller than the freestream velocity. For example for a freestream velocity of 10 m/s,  $We^+$  is in the range  $5 \times 10^{-3}$  to  $7 \times 10^{-3}$  for typical boundary layers. Assuming the midpoint value of  $We^+ = 6 \times 10^{-3}$ , figure 15(a) predicts  $L_{crit}^+ \sim 50$ , which is dimensionally on the order of  $L = 50\nu/u_\tau \sim 100$  microns. Figure 15(c) predicts that for this  $We^+$  the maximum achievable slip velocity is about 12 in plus units.

We note that the developed model predicts an upper bound for robustness of superhydrophobic surfaces, by only considering one failure mechanism. Other failure modes such as hydrostatic pressure (if not treated) and gas dissolutions (if exposed to water for long time) should be considered in addition to what was presented here.

Lastly, we note that the presented model uses only a one way coupled system, and ignores the effects of interface deformation back on the flow field. A more accurate analysis should include interface dynamics fully coupled with the flow. Preliminary investigations indicate that pressure fluctuations in a fully coupled system are slightly higher than those in the one-way coupled systems considered here (Seo *et al.* 2014). Therefore, reaffirming the fact that the developed model predicts only an upper bound for the stable SHS operation.

## 5. Summary and Discussion

The presented work investigated dynamics of turbulent flows over superhydrophobic textured walls with entrapped gas pockets. We presented for the first time simulations for a wide range of scales for a three-dimensional texture geometry: from small textures on the order of  $L^+ = 6$  to very large textures with  $L^+ = 155$ . We showed that the small texture limit, results in slip velocity predicted by linear theory of Ybert *et al.* (2007), and found the threshold of validity of linear theory to be around  $L^+ \sim 10$ .

We presented three dimensionless parameters that describe the system. These are boundary layer Reynolds number,  $Re_\tau$ , texture dimension in viscous units,  $L^+$ , and Weber number in viscous units,  $We^+ = \rho u_\tau \nu / \sigma$ . The defined Weber number is convenient since it is dominantly controlled by the freestream velocity, and allows easier communication of our results in terms of dimensional parameters. Furthermore, it does not assume any *a priori* scaling of pressure with  $L^+$ , and with these parameters, all texture dependent effects are controlled through a single dimensionless parameter,  $L^+$ .

By investigating different Reynolds numbers, we showed that deviation in flow statistics due to texture is independent of Reynolds number when plotted in terms of inner

dimensions. Furthermore, texture effects penetrate up to  $y^+$  of order  $\sim 60$ , and beyond this point, the profiles are very similar to smooth-wall turbulent boundary layers. These findings helped establishing the relevance of our calculations to higher Reynolds number flows.

We investigated pressure fluctuations in terms of two modes: an unsteady turbulent mode and a steady coherent mode solely controlled by the texture geometry. While the pressure magnitude of the turbulent mode is of the same order of that in a smooth-wall turbulent boundary layer, the pressure field associated with the texture geometry was shown to significantly increase with the texture size. Particularly for three-dimensional post geometry this pressure increase was more significant (in comparison to two-dimensional streamwise ridges) due to the stagnation of slip velocity with the edge of the posts. We showed that the coherent pressure field has a self similar behavior for a wide range of  $L^+$ , and that it scales linearly with the slip velocity. Lastly, we performed analysis of interface deformation due to the resulting pressure fields and predicted threshold conditions for interface failure and transition to the Wenzel state. Combining the knowledge of pressure fluctuations and interface deformation, it becomes clear that the implementation of large textures can deteriorate the stability of the gas pockets. This is observed in various experiments (Aljallis *et al.* 2013; Bidkar *et al.* 2014), but not predicted by the state-of-the-art simulations. The present results may discourage further focus on post layouts, and indeed most recent studies have focused on ridges (Daniello *et al.* 2009; Woolford *et al.* 2009; Park *et al.* 2014). However, streamwise ridges are only implementable in academic scenarios. In practice, the fabrication of perfectly aligned ridges is complicated and expensive. Moreover, ridge geometries can suffer the same stagnation issues, when misaligned to the flow direction. On the other hand, in the small-wavelength limit of practical applications,  $L^+ \approx 5$ , the stagnation effect is small and posts become an attractive option. In this limit, slip velocities of order  $U_s^+ \simeq 3$  are still achievable, implying drag reductions order of 15%. Post geometries are also more similar to realistic superhydrophobic surfaces involving more practical ways for mass production, such as the randomly distributed roughness spray coatings recently tested in Aljallis *et al.* (2013), Bidkar *et al.* (2014), and Srinivasan *et al.* (2015). Their observations agree qualitatively with the deterioration of the stability of the gas pockets reported here.

This work was supported by the Office of Naval Research under grant 3002451214. The authors greatly appreciate the Kwanjeong Educational Foundation for the funding support for Jongmin Seo.

## Appendix A. Convergence of statistics with respect to the computational domain size

We present here briefly a comparison of DNS statistics obtained from simulations over different domain sizes. To guide the critical directions over which we should change the domain, we first performed an analysis of correlation statistics in both streamwise and spanwise directions for all three components of the velocity field. As shown in figure 16 with the exception of  $R_{uu}$  as a function of streamwise separation distance all other correlations show a satisfactory drop to zero. This indicates that a convergence study is needed in which the domain size is changed in the streamwise direction.

We performed a new calculation for the presented case, in which the streamwise domain is doubled to  $D_x = 4\pi$ . Figure 17 shows that for this case all correlations drop satisfactorily to zero. Figure 18 confirms that the velocity statistics are not affected with the change in the domain size. Specifically, the mean flow rate was within 0.25% difference between the two calculations and the slip velocity was within 0.5% difference.

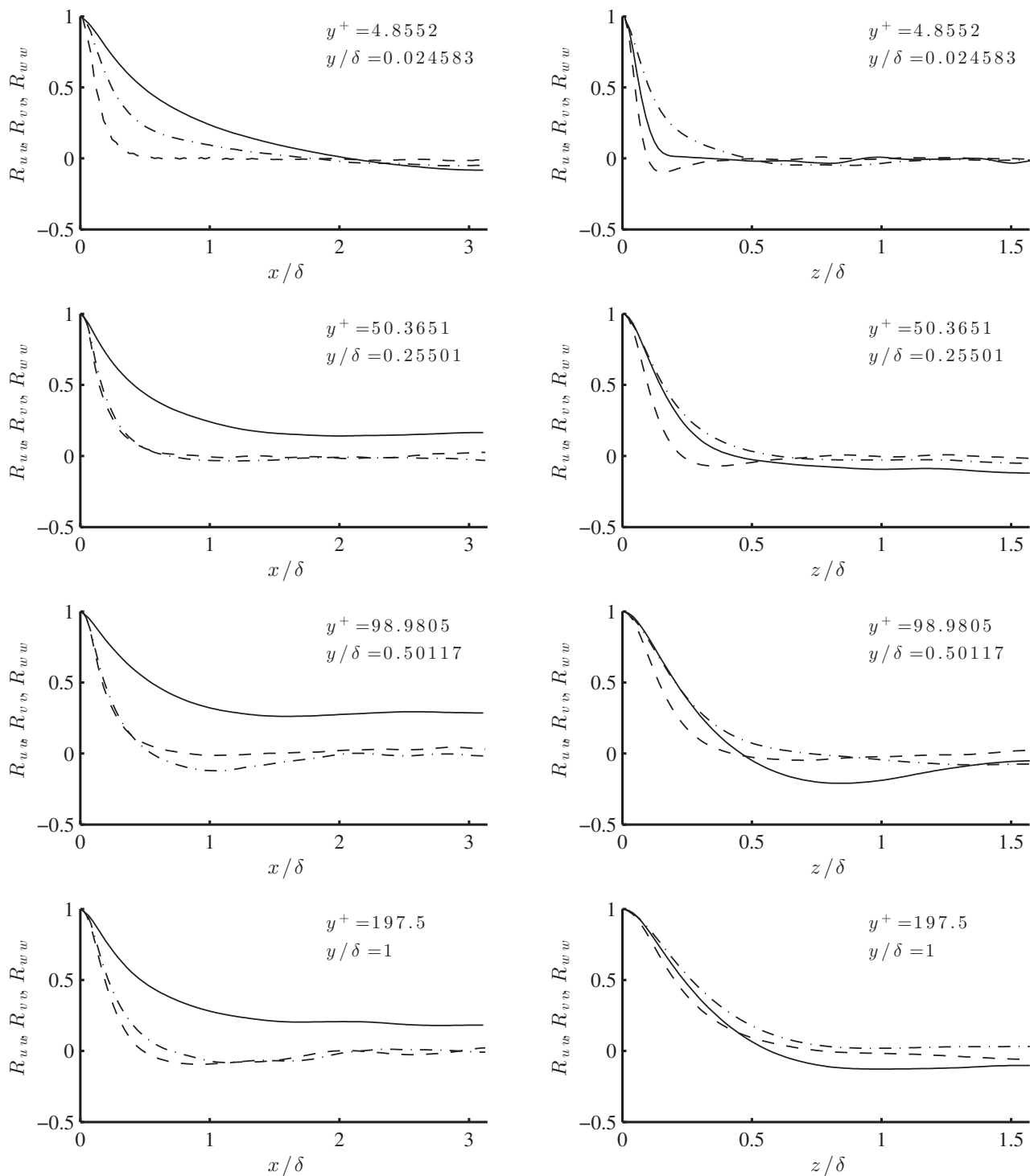


FIGURE 16. Two-point correlations along streamwise(left column) and spanwise(right column) directions for  $L^+ \approx 155$ ,  $D_x = 2\pi$ , and  $D_z = \pi$ ; —,  $R_{uu}$ , ----,  $R_{vv}$ , - · - ·,  $R_{ww}$ .

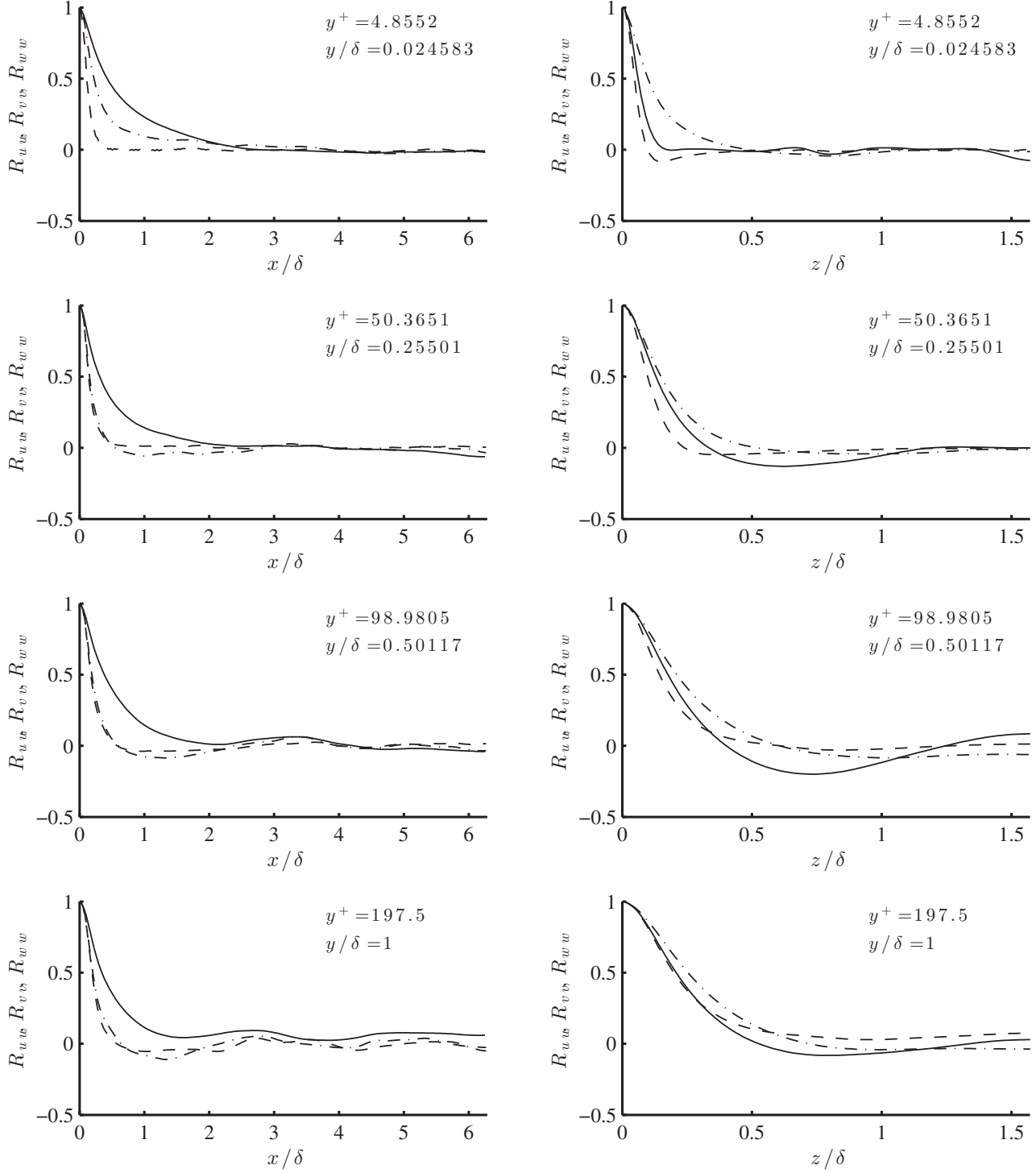


FIGURE 17. Two-point correlations along streamwise(left column) and spanwise(right column) directions for  $L^+ \approx 155$ ,  $D_x = 4\pi$ , and  $D_z = \pi$ ; —,  $R_{uu}$ , ----,  $R_{vv}$ , - · -,  $R_{wv}$ .

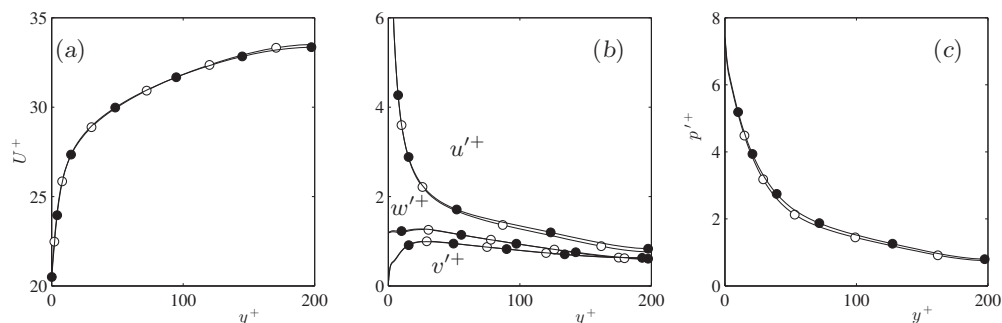


FIGURE 18. Comparison of statistics for  $L^+ \approx 155$  at  $Re_\tau \approx 200$ . (a) Mean streamwise velocity profile; (b) velocity rms fluctuations; (c) pressure rms fluctuations.  $\bullet$ , domain size  $D_x = 2\pi, D_z = \pi$ ;  $\circ$ , domain size  $D_x = 4\pi, D_z = \pi$

## REFERENCES

- ALJALLIS, E., SARSHAR, M. A., DATLA, R., SIKKA, V. & JONE, A. 2013 Experimental study of skin friction drag reduction on superhydrophobic flat plates in high Reynolds number boundary layer flow. *Phys. Fluids* **25**, 025103.
- BELYAEV, A. V. & VINOGRADOVA, O. I. 2010 Effective slip in pressure-driven flow past superhydrophobic stripes. *J. Fluid Mech.* **652**, 489–499.
- BIDKAR, RAHUL A., LEBLANC, LUC, KULKARNI, AMBARISH J., BAHADUR, VAIBHAV, CECCIO, STEVEN L. & PERLIN, MARC 2014 Skin-friction drag reduction in the turbulent regime using random-textured hydrophobic surfaces. *Phys. Fluids* **26**, 085108.
- BOSE, S. T., MOIN, P. & YOU, D. 2010 Grid-independent large-eddy simulation using explicit filtering. *Phys. Fluids* **22**, 105103.
- BUSSE, A. & SANDHAM, N. D. 2012 Influence of an anisotropic slip-length boundary condition on turbulent channel flow. *Phys. Fluids* **24**, 055111.
- BUSSE, A. & SANDHAM, N. D. 2013 Turbulent flow over superhydrophobic surfaces - roughness versus slip. In *14TH European Turbulence Conference*. Lyon, France.
- CASSIE, A. B. D. & BAXTER, S. 1944 Wettability of porous surfaces. *Trans. Faraday Soc.* **40**, 546–551.
- CHOI, C.-H. & KIM, C.-J. 2006 Large slip of aqueous liquid flow over a nanoengineered superhydrophobic surface. *Phys. Rev. Lett.* **96**, 066001.
- CHOI, C.-H., ULMANELLA, U., KIM, J., HO, C.-M. & KIM, C.-J. 2006 Effective slip and friction reduction in nanogated superhydrophobic microchannels. *Phys. Fluids* **18**, 087105.
- CHOI, HAECHEON, MOIN, PARVIZ & KIM, JOHN 1993 Direct numerical simulation of turbulent flow over riblets. *J. Fluid Mech.* **255**, 503–539.
- CLAUSER, F.H. 1956 The turbulent boundary layer. *Advances Appl. Mech.* **4**, 1–51.
- DANIELLO, R., WATERHOUSE, N. E. & ROTHSTEIN, J. P. 2009 Turbulent drag reduction using superhydrophobic surfaces. *Phys. Fluids* **21**, 085103.
- FREUND, J. B. 2003 The atomic detail of a wetting/de-wetting flow. *Phys. Fluids* **15**, L33–36.
- FUKAGATA, K., KASAGI, N. & KOUMOUTSAKOS, P. 2006 A theoretical prediction of friction drag reduction in turbulent flow by superhydrophobic surfaces. *Phys. Fluids* **18**, 051703.
- GARCÍA-MAYORAL, R. & JIMÉNEZ, J. 2011a Drag reduction by riblets. *Phil. Trans. R. Soc. A* **369**, 1412–1427.
- GARCÍA-MAYORAL, R. & JIMÉNEZ, J. 2011b Hydrodynamic stability and breakdown of the viscous regime over riblets. *J. Fluid Mech.* **678**, 317–347.
- GARCÍA-MAYORAL, R. & JIMÉNEZ, J. 2012 Scaling of turbulent structures in riblet channels up to  $Re_\tau \approx 550$ . *Phys. Fluids* **24**, 105101.
- HOYAS, S. & JIMÉNEZ, J. 2006 Scaling of the velocity fluctuations in turbulent channels up to  $Re_\tau = 2003$ . *Phys. Fluids* **18**, 011702.
- HYVÄLUOMA, J. & HARTING, J.D.R. 2008 Slip flow over structured surfaces with entrapped microbubbles. *Phys. Rev. Lett.* **100**, 246001.
- JELLY, T. O., JUNG, S. Y. & ZAKI, T. A. 2014 Turbulence and skin friction modification

- in channel flow with streamwise-aligned superhydrophobic surface texture. *Phys. Fluids* **26** (095102).
- JIMÉNEZ, J. 1994 On the structure and control of near wall turbulence. *Phys. Fluids* **6** (2), 944–953.
- JIMÉNEZ, J. 2004 Turbulent flows over rough walls. *Ann. Rev. Fluid Mech.* **36**, 173–196.
- JIMÉNEZ, J., UHLMAN, M., PINELLI, A. & G., KAWAHARA 2001 Turbulent shear flow over active and passive porous surfaces. *J. Fluid Mech.* **442**, 89–117.
- KAMRIN, KEN, BAZANT, MARTIN Z. & STONE, HOWARD A. 2010 Effective slip boundary conditions for arbitrary periodic surfaces: the surface mobility tensor. *J. Fluid Mech.* **658**, 409–437.
- KARATAY, ELIF, HAASE, A. SANDER, VISSER, CLAAS WILLEM, SUN, CHAO, LOHSE, DETLEF, TSAIA, PEICHUN AMY & LAMMERTINK, ROB G. H. 2013 Control of slippage with tunable bubble mattresses. *PNAS* **110** (21), 8422–8426.
- KIM, J. & MOIN, P. 1985 Application of a fractional step method to incompressible Navier-Stokes equations. *J. Comput. Phys.* **59**, 308–323.
- LAUGA, J. & STONE, H. 2003 Effective slip in pressure-driven Stokes flow. *J. Fluid Mech.* **489**, 55–77.
- LEE, C. & KIM, C.-J. 2009 Maximizing the giant liquid slip on superhydrophobic microstructures by nanostructuring their sidewalls. *Langmuir* **25**, 12812–12818.
- LEE, MYOUNGKYU & MOSER, ROBERT D. 2015 Direct numerical simulation of turbulent channel flow up to  $Re_\tau = 5200$ . *J. Fluid Mech.* **774**, 395–415.
- LOZANO-DURÁN, ADRIÁN & JIMÉNEZ, JAVIER 2014 Effect of the computational domain on direct simulations of turbulent channels up to  $Re_\tau = 4200$ . *Phys. Fluids* **26**, 011702.
- LUCHINI, P. 1996 Reducing the turbulent skin friction. In *Computational Methods in Applied Sciences '96* (ed. J.-A. Desideri et al.), pp. 466–470. Wiley.
- LUCHINI, P., MANZO, F. & POZZI, A. 1991 Resistance of a grooved surface to parallel flow and cross-flow. *J. Fluid Mech.* **228**, 87–109.
- MARTELL, M. B., PEROT, J. B. & ROTHSTEIN, J. P. 2009 Direct numerical simulations of turbulent flows over superhydrophobic surfaces. *J. Fluid Mech.* **620**, 31–41.
- MARTELL, M. B., ROTHSTEIN, J. P. & PEROT, J. B. 2010 An analysis of superhydrophobic turbulent drag reduction mechanisms using direct numerical simulation. *Phys. Fluids* **22**, 065102.
- MIN, T. & KIM, J. 2004 Effects of hydrophobic surface on skin-friction drag. *Phys. Fluids* **16**, L55–L58.
- MIN, T. & KIM, J. 2005 Effects of hydrophobic surface on stability and transition. *Phys. Fluids* **17**, 108106.
- MORINISHI, Y., LUND, T. S., VASILYEV, O. V. & MOIN, P. 1998 Fully conservative higher order finite difference schemes for incompressible flow. *J. Comput. Phys.* **143**, 90–124.
- MOSER, R., KIM, J. & MANSOUR, N. 1998 Direct numerical simulation of turbulent channel flow up to  $Re_\tau \approx 590$ . *Phys. Fluids* **11**, 943–945.
- OU, J., PEROT, J. B. & ROTHSTEIN, J. P. 2004 Laminar drag reduction in microchannels using ultrahydrophobic surfaces. *Phys. Fluids* **16**, 4635–4643.
- PARK, H., PARK, H. & KIM, J. 2013 A numerical study of the effects of superhydrophobic surface on skin-friction drag in turbulent channel flow. *Phys. Fluids* **25**, 110815.
- PARK, H., SUN, G. & KIM, C.-J. 2014 Superhydrophobic turbulent drag reduction as a function of surface grating parameters. *J. Fluid Mech.* **747**, 722–734.
- PATANKAR, N. A. 2010 Consolidation of hydrophobic transition criteria by using an approximate energy minimization approach. *Langmuir* **26**, 8941–8945.
- REYNOLDS, W.C. & HUSSAIN, A.K.M.F. 1972 The mechanics of an organized wave in turbulent shear flow. part 3.theoretical models and comparisons with experiments. *J. Fluid Mech.* **54**, 263–288.
- ROTHSTEIN, J. P. 2010 Slip on superhydrophobic surfaces. *Annu. Rev. Fluid Mech.* **42**, 89–109.
- SAMAHA, M. A., VAHEDI, T. H. & EL HAK, M. GAD 2011 Modeling drag reduction and meniscus stability of superhydrophobic surface of random roughness. *Phys. Fluids* **23**, 012001.
- SEO, J., GARCÍA-MAYORAL, R. & MANI, A. 2013 Pressure fluctuations in turbulent flows over superhydrophobic surfaces. *CTR Ann. Res. Briefs* pp. 217–229.
- SEO, J., GARCÍA-MAYORAL, R. & MANI, A. 2014 Turbulent flows over superhydrophobic sur-

- faces: gas-liquid interface dynamics. *30th Symposium on Naval Hydrodynamics Hobart, Australia* .
- SPALART, P. R. & MCLEAN, J. D. 2011 Drag reduction: enticing turbulence, and then an industry. *Phil. Trans. R. Soc. A* **369**, 1556–1569.
- SRINIVASAN, SIDDARTH, KLEINGARTNER, JUSTIN A., GILBERT, JONATHAN B., COHEN, ROBERT E., MILNE, ANDREW J. B. & MCKINLEY, GARETH H. 2015 Sustainable drag reduction in turbulent taylor-couette flows by depositing sprayable superhydrophobic surfaces. *Phys. Rev. Lett.* **114**, 014501.
- STEINBERGER, AUDREY, CILE COTTIN-BIZONNE, CE, KLEIMANN, PASCAL & CHARLAIX, ELISABETCH 2007 High friction on a bubble mattress. *Nature Materials* **6**, 665–668.
- TEO, C. J. & KHOO, B. C. 2010 Flow past superhydrophobic surfaces containing longitudinal grooves: effects of interface curvature. *Microfluidics and Nanofluidics* **9**, 499–511.
- THOMPSON, P. A. & TROIAN, S. M. 1997 A general boundary condition for liquid flow at solid surfaces. *Nature* **389**, 360–362.
- TÜRK, S., DASCHIEL, G., STROH, A., HASEGAWA, Y. & FROHNAPFEL, B. 2014 Turbulent flow over superhydrophobic surfaces with streamwise grooves. *J. Fluid Mech.* **747**, 186–217.
- VAN DYKE, MILTON 1962 Higher approximations in boundary-layer theory part 1. general analysis. *J. Fluid Mech.* **14**, 161–177.
- WATANABE, K., YANUAR & UDAGAWA, H. 1999 Drag reduction of newtonian fluid in a circular pipe with highly water-repellent wall. *J. Fluid Mech.* **381**, 225–238.
- WENZEL, R. N. 1936 Resistance of solid surfaces to wetting by water. *Ind. Eng. Chem.* **28**, 988–994.
- WOOLFORD, B., PRINCE, J., MAYNES, D. & WEBB, B. W. 2009 Partical image velocimetry characterization of turbulent channel flow with rib patterned superhydrophobic walls. *Phys. Fluids* **21**, 085106.
- YBERT, C., BARENTIN, C. & COTTIN-BIZONNE, C. 2007 Achieving large slip with superhydrophobic surfaces: Scaling laws for generic geometries. *Phys. Fluids* **19**, 123601.